CrossMark

The nonlinear effects of the eddy viscosity and the bottom friction on the Lagrangian residual velocity in a narrow model bay

Fangjing Deng[1] · Wensheng Jiang[1,2] · Shizuo Feng[1]

Abstract The nonlinear effects of the eddy viscosity and the bottom friction on the Lagrangian residual velocity (LRV) are studied numerically in a narrow model bay. Three groups of the experiments with different eddy viscosity and different forms of the bottom friction are designed and are carried out in the three kinds of the topography. When the eddy viscosity is obtained from a two-equation turbulence closure model, the pattern of the LRV is more complex than that of the time invariant eddy viscosity case and the intensity is from more than 1.3 times to one order smaller than that of the linear eddy viscosity condition. The LRV are also acquired when the eddy viscosity varies from the flood-averaged one to the ebb-averaged one. It is found that when the flood-averaged eddy viscosity is bigger than the ebb-averaged eddy viscosity (flood-dominated asymmetry), the direction of the breadth-averaged LRV and the 3D LRV is nearly opposite to that when the eddy viscosity asymmetry is reverse (ebb-dominated asymmetry). However, the intensity of the LRV for the ebb-dominated case decreases toward the flood-dominated case as the ratio of the maximum depth in the deep channel and the minimum depth on the shoal increases. The different forms of the bottom friction also play a role in the LRV. The structures of the 3D LRV and the depth-integrated LRV are simpler, and the intensity of the LRV is two times smaller when the linear bottom friction is used than those when the quadratic bottom friction is used.

1 Introduction

When tide is the main driving force in bays and channels, not only the nonlinear advection but also the temporally varying eddy viscosity and the nonlinear bottom friction can generate residual current. There mainly exist two categories of the definition of the residual currents, namely the Eulerian residual velocity (ERV) and the Lagrangian residual velocity (LRV). The ERV was obtained by averaging the current velocity in one or several tidal periods at a fixed location (Abbott 1960). The LRV was defined by Zimmerman (1979) as the net displacement of a labeled water parcel over one or several tidal periods. Feng et al. (1986a) proved that under the weakly nonlinear condition, the LRV was equal to the sum of the ERV and the Stokes' drift velocity.

In many studies, the nonlinear effects of the eddy viscosity are always neglected when studying the generation mechanism of the residual current. When the ERV is used as the representative of the residual current, Hansen and Rattray (1965) established the estuary dynamics theory by assuming a time-invariant eddy viscosity coefficient. This theory was applied in many estuaries and achieved a lot of success, while the contradiction of the time-invariant eddy viscosity and the large fluctuation of it during the tidal cycle is always a problem.

Simpson et al. (1990) found that the periodical stratification in the estuary caused by the tidal current leads to the periodical variation of the turbulence intensity, which they called the tidal straining. Jay and Musiak (1994, 1996) also found the similar phenomenon which they called the internal tidal

✉ Wensheng Jiang
   wsjang@ouc.edu.cn

   Fangjing Deng
   fangjingdeng@yahoo.com

   Shizuo Feng
   szfeng@ouc.edu.cn

[1] Physical Oceanography Laboratory/CIMST, Ocean University of China and Qingdao National Laboratory for Marine Science and Technology, Qingdao, China

[2] Laboratory of Marine Environment and Ecology, Ocean University of China, Qingdao, China

asymmetry. They all found that this effect intensifies the estuarine circulation. Burchard and Hetland (2010) investigated the contribution of the tidal straining effect numerically by solving the rectilinear tidal motion subject to a constant longitudinal buoyancy gradient. They found that the tidal straining induced circulation is larger than the gravitational circulation. The subsequent studies also confirmed the above finding (Burchard et al. 2011, 2014; Burchard and Schuttelaars 2012). Cheng et al. (2010, 2013) and Cheng (2014) also obtained the similar results by taking more processes into consideration.

In the above studies, the ERV is used as the residual circulation velocity. However, it has been proven in Feng et al. (2008) that the ERV does not satisfy the material surface conservation law which was pointed out in Lamb (1975) as a general surface condition. While the LRV satisfies that law and is suitable for representing the residual circulation velocity. There are also many studies on the generation mechanism of the LRV in the shallow seas. Ianniello (1977) gave the first analytical solution of the LRV which showed that the LRV is against the gravitational circulation in a breadth-averaged model by summing up the ERV and the Stokes' drift velocity. Winant (2008) calculated the LRV by using the same approach to get the 3D LRV in a narrow bay analytically. The results showed that the ratio of the dissipative frequency and the tidal frequency have obvious effects on the 3D LRV, whose structures with larger ratio were much simpler than those with smaller one. Jiang and Feng (2014) analytically derived the 3D LRV again by solving the LRV governing equations directly. They found that if the flat sea bottom is assumed, their results can be retreated to Ianniello's (1977) results. In the nonflat bottom case, the breadth-averaged LRV showed a more complex pattern which enhances the gravitational circulation. In all of these analytical studies, the temporally constant eddy viscosity and the no-slip bottom condition were assumed, which ignored the nonlinear effects of both the eddy viscosity and the bottom friction. Feng and Lu (1993) have derived the LRV governing equations with a simplified turbulence closure model to demonstrate the nonlinear effect of the eddy viscosity on the LRV. It was found that the time-variant eddy viscosity induced a generation term in the LRV governing equations no matter what is the mechanism to generate this time dependence. However, they only gave the theoretical framework and no solution has been obtained.

Apart from the eddy viscosity, the bottom friction is also an important source of the nonlinearity to the LRV. Jiang and Feng (2011) examined its performance in a depth-averaged analytical model. Although the linear bottom friction was assumed to get the analytical result, the bottom friction term in the momentum equations contains the instantaneous water depth which makes this term a nonlinear one. Hence, they found that the bottom friction has two contradictory effects, one is to damp the LRV and the other is to generate it. Quan et al. (2014) further explored this problem by using the depth-

averaged numerical model and found that the quadratic bottom friction contributes more complexity to the LRV than the linear bottom friction. However, the corresponding study in 3D condition has not been reported.

In the present study, the effects of the temporal variation of the eddy viscosity (nonlinear effects of eddy viscosity) and the nonlinear effects of the bottom friction on the 3D LRV will be examined by applying the numerical model in a rectangular bay. The 3D LRV is obtained by setting different turbulence closure schemes and different forms of the bottom friction in the model. Their variations with the turbulence closure schemes and the bottom friction forms are acquired. The paper is arranged as follows. The methods and the model configuration will be given in section 2. The results and discussions are shown in the section 3. Finally, the conclusions are reached in section 4.

2 Methods and the model configuration

2.1 The model description and its setup

The Finite-Volume Coastal Ocean Circulation Model (FVCOM) is used to carry out the experiments in an idealized setting. The model is a 3D unstructured-grid, free-surface, primitive equations ocean model that uses the sigma coordinate and the arbitrarily sized triangular mesh (Chen et al. 2003). In FVCOM, several options of the turbulence closure scheme can be chosen which includes the Mellor and Yamada (1982) level 2.5 (MY-2.5) turbulence closure model, k-ε model, and the constant eddy viscosity coefficient scheme. In order to carry out the experiment in the present study, a new option is added in FVCOM to allow the input of the vertical profiles of the eddy viscosity coefficients on each grid point at each time step. The original bottom friction form is the quadratic bottom friction in FVCOM, and the code is modified to include the option of the linear bottom friction form.

The model domain in this study is a semi-enclosed rectangular bay. A Cartesian coordinate system is set up in the model bay with the x-axis being along the bay (the head of bay is at $x = 0$ and the open boundary is at $x = L$) and the y-axis being across the bay ($y = 0$ and $y = B$ are the two lateral boundaries). The topography varies only in y direction, and the lateral depth profile is expressed as:

$$h = a + b \times e^{-((2y/1000-20)/7)^2} \tag{1}$$

where a, b are two parameters to control the topography. The topography described in Eq. (1) is quite typical for a coastal narrow bay, which has two shoals along the two sides of the bay and a deep part in the center. In the present study, three kinds of the topography are used with a being 5 m and b being 5, 10, and 15 m respectively, which reflects the different steepness of the bottom. The bay length L is chosen as 0.3

wavelengths or 1 wavelength of the incoming tide to simulate the short and the long bay. Then the bay length is roughly 120 km or 400 km when $a = 5$ m, $b = 10$ m are taken and the M_2 tide is assumed. The bay width B is chosen as 20 km; thus, the narrow bay case is studied in this paper, so the Coriolis force can be omitted in the present study.

No freshwater discharge is imposed at the head of the bay, only the semidiurnal tide (M_2) with the amplitude of 1 m is imposed at the open boundary. The density is constant in the bay to study the barotropic case only.

In the present system, the basic characteristic scales are $x_c = \lambda_c$, $y_c = B$, $z_c = h_c$, and $T_c = \omega^{-1}$, where $h_c = 8.1$ m is the mean depth of the bay obtained from Eq. (1) with $a = 5$ m and $b = 10$ m, $\omega = 1.4 \times 10^{-4}$ s^{-1} is the tidal frequency for the M_2 tide, and $\lambda_c = 2\pi\sqrt{gh_c}T_c$ is the tidal wavelength. In view of the tidal dynamics in the present model domain, the characteristic velocity scales are $u_c = \zeta_c\sqrt{g/h_c}$, $v_c = B\zeta_c/(h_cT_c)$, $w_c = \zeta_c/T_c$, where $\zeta_c = 1$ m is the scale of the tidal amplitude. The scale analysis in the present study is after Jiang and Feng (2014), and it is nearly the same as those in Winant (2008). The only difference is that the tidal wavelength is taken as the horizontal scale in the present study, while in Winant (2008) the bay length was chosen as the horizontal scale. However, in both studies, these two scales are of the same order.

The resolution of the model grid is around 50 m near the head of the bay and is 1000 m near the open boundary, and the vertical layers are uniformly divided into 15 sigma layers. The model runs for 5 days until it reaches the steady state. Then the results of the last tidal period of the simulation are used for further manipulation.

2.2 The calculation method for the LRV

The LRV is calculated according to its original definition, which is the net displacement of the water parcels over one or several tidal periods (Zimmerman 1979). Feng et al. (2008) proved that the so obtained velocity can formulate the velocity field only when the net displacement is at least one order smaller than the length scale of the flow field. The x-direction, y-direction, and z-direction components of the LRV are (u_{LR}, v_{LR}, w_{LR}), which is listed as follows:

$$
\begin{aligned}
u_{LR} &= \frac{1}{nT} \int_{t_0}^{t_0+nT} u(\mathbf{x}(t; \mathbf{x}_0, t_0), t)dt \\
v_{LR} &= \frac{1}{nT} \int_{t_0}^{t_0+nT} v(\mathbf{x}(t; \mathbf{x}_0, t_0), t)dt \quad (2) \\
w_{LR} &= \frac{1}{nT} \int_{t_0}^{t_0+nT} w(\mathbf{x}(t; \mathbf{x}_0, t_0), t)dt
\end{aligned}
$$

where ($\mathbf{x}_0$, t_0) is the initial position and the starting time of the labeled parcel. The $\mathbf{x}(t; \mathbf{x}_0, t_0)$ is the position of that water parcel at the time of t, which represents the trajectory of the water parcel starting from $\mathbf{x}_0$ at the time of t_0. Here, (u, v, w) are the tidal currents along the x, y, and z-axes, which is in the geopotential coordinates (z-coordinate). In this paper, only one tidal period will be tracked for every parcel; thus, $n = 1$ is assumed.

The equations solved in FVCOM are based on the sigma coordinate, with its axes being x_σ, y_σ, and σ. However, the velocities calculated in the equations are u, v, and ω_σ, with u, v being the velocities along the x-axis and y-axis in z-coordinate, respectively, and ω_σ being along the σ-axis in sigma-coordinate. In FVCOM the vertical velocity w in the z-coordinate is also provided as an output option. The velocities (u, v, w) are obtained at sigma layers in the present study. Then, the water parcels are tracked in geopotential coordinate by applying the 4th order Runger-Kutta scheme and the 3D LRV is obtained according to Eq. (2).

In the present study, the 3D LRV, depth-integrated LRV, and the breadth-averaged LRV are calculated. In order to obtain the detailed information of each variable, two kinds of the initial water parcel arrangements are used. For the 3D LRV and the depth-integrated LRV, the initial water parcels are chosen on every model grid which is on the sigma layer. This can guarantee the same vertical resolution in the whole model area. When the breadth-averaged LRV is acquired, the initial water parcels are chosen according to its z-level so that for every cross-section, all the LRV are defined at the same level to ensure that the breadth-averaging procedure can be carried out. In this study, in the vertical direction, the initial position of the water parcels is set 1 m apart.

2.3 The model validation

In order to test the validity of the model, a test case based on the setup of the analytical study in Jiang and Feng (2014) is carried out. The system in Jiang and Feng (2014) is a weakly nonlinear case in a narrow bay so that they can obtain the analytical solution by using the perturbation method. In the present study, the geometry of the model area and the driving force are both taken from Jiang and Feng (2014). It forms the basis for the comparison between these two studies.

In Jiang and Feng (2014), the vertical eddy viscosity v_c was regarded as a constant. In order to estimate that constant, they set $\delta_e = 1$, where the nondimensional number $\delta_e = v_c/(h_c^2\omega)$ is defined as the ratio of the dissipative frequency (v_c/h_c^2) and the tidal frequency (ω) which measures the relative importance of the eddy viscosity term and the local acceleration term in the governing equations. It corresponds to $v_c = 0.009$ m^2/s which is also adopted in the test experiment in the present study.

In view of the feasibility to get the analytical solution, the no-slip bottom boundary condition is adopted in Jiang and Feng (2014). According to Eq. (82) of that paper, the effect of the no-slip bottom boundary condition is equivalent to the linear form of the bottom friction. Based on the model setting in Jiang and Feng (2014), the linear bottom friction coefficient (β_T) was estimated as 0.01 m/s which is also used in the validation run. Thus, the test experiment here can be compared essentially with that in Jiang and Feng (2014).

Figure 1 is the nondimensional LRV of the four cross-sections in the 0.3 wavelength long bay, which shows that the LRV are landward from the upper layers of the deep channel and seaward from the both sides and the bottom layers of the bay. The results in Fig. 2 are the streamlines of the depth-integrated LRV in the 0.3 wavelength long bay, which shows that the LRV flows inside from the deep channel and outside from the both sides of the bay. The characteristics of them are the same as Fig. 1 ($L = 0.3$) and Fig. 3a in Jiang and Feng (2014). It demonstrates that the model is reliable to calculate the LRV by using the procedure described in section 2.2.

2.4 The design of the experiments

In order to study the effects of the nonlinear eddy viscosity on the LRV and the influence of the different forms of the bottom friction, three groups of the numerical experiments are designed in the present study. They are listed as follows:

(1) For the first group, the experiments are designed to compare the difference of the LRV when the linear and the nonlinear eddy viscosity are used in the FVCOM model. There are four experiments in this group. The first case is that the eddy viscosity in the FVCOM model is

calculated by the turbulence closure model of Mellor and Yamada (1982), which is called the "MY-2.5 model case" hereafter. The second case is that the eddy viscosity used is the tidal average of the eddy viscosity in the first case, which is called the "tidally averaged case." In this case, the eddy viscosity is time invariant but it still has horizontal and vertical structures. The third case is that the eddy viscosity from the first case is temporally and vertically averaged, which is called the "tidally-vertically averaged case." Thus, it only has horizontal structures. The fourth case is that the eddy viscosity is temporally and spatially averaged in the whole bay and it is a constant value, which is called the "constant eddy viscosity case." In the first case, the nonlinear eddy viscosity effect is included in the model, while in the latter three cases the eddy viscosity term is only linear.

(2) The eddy viscosity varies with the tidal phase, and the major difference exists between the flood and the ebb tide. Two kinds of the asymmetry between the flood-averaged and the ebb-averaged eddy viscosity are considered in the present paper to study their effect. One is the flood-dominated asymmetry with the flood-averaged eddy viscosity being larger than the ebb-averaged eddy viscosity, and another is the ebb-dominated asymmetry with the latter being larger than the former. Thus, two sensitivity experiments are designed in this group to represent the two different types of the asymmetry, one for the flood-dominated asymmetry and the other one for the ebb-dominated asymmetry.

(3) In order to compare the effect of the bottom friction, two forms of the bottom friction are used, which are the quadratic bottom friction $C_d = \sqrt{u^2 + v^2}(u, v)$ and the linear bottom friction $\beta_T(u, v)$. The C_d is the quadratic bottom drag coefficient and the β_T is the linear bottom friction coefficient.
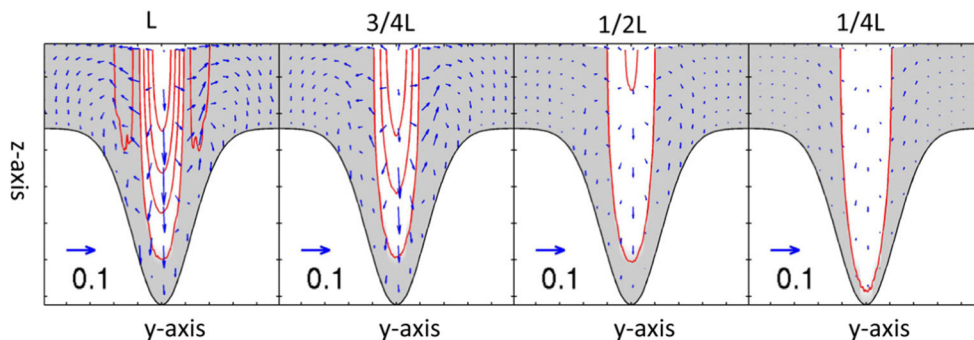

Fig. 1 The nondimensional LRV of four cross sections in the 0.3 wavelength long bay with $a = 5$ m, $b = 10$ m for constant eddy viscosity case with the linear bottom friction ($\beta_T = 0.01$ m/s). *Shaded areas* denote the positive values (outflow toward the ocean), while the *blank areas* denote the negative values (inflow toward the head) of the velocity along the *x*-axis. The *red contour lines* represent the magnitude of the velocity along the *x*-axis and the contour interval is 0.02. The *blue vectors* are the magnitude and direction of the lateral and the vertical velocity

Fig. 2 The streamlines of the depth-integrated LRV in the 0.3 wavelength long bay with $a = 5$ m, $b = 10$ m for the constant eddy viscosity case with the linear bottom friction ($\beta_T = 0.01$ m/s)
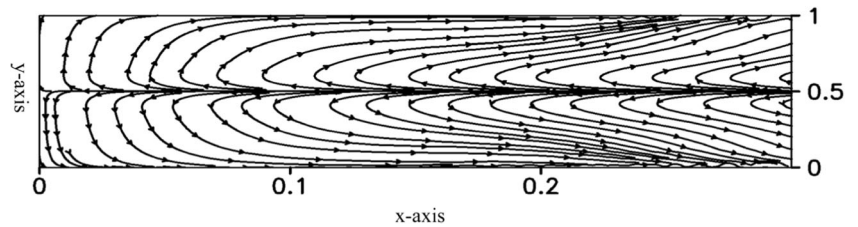
3 Results and discussions

The three groups of the numerical experiments described in section 2.4 are carried out under three kinds of the topography condition described in Eq. (1) by varying the parameters a and b. The results show that the patterns of the LRV are not sensitive to the variation of the topography set in the present study. This is because in the range of the variation of the topography, the nondimensional parameter δ_e does not change its order of magnitude. Hence, the LRV under the topography with $a=$ 5 m, $b=10$ m will be exhibited hereafter in the present study.

However, the intensity of the LRV under different topography conditions has different variations as the ratio of the maximum depth in the deep channel and the minimum depth on the shoal changes. We set the length of the bay to 120 km and vary the topography only to study the change of the LRV intensity due to the topography. The dimensional results are shown in Table 1 and discussed in each subsection below.

3.1 The comparison between the nonlinear eddy viscosity and the linear eddy viscosity

As described in section 2.4, the turbulence closure model of Mellor and Yamada (1982) is used in the FVCOM model to calculate the tidal current, and the time varying eddy viscosity is also acquired. It shows that the eddy viscosity has obvious temporal and spatial distributions. It appears that in the vertical direction, the eddy viscosity shows a higher value at the middle of the water column and lower value near the surface and the bottom, and the eddy viscosity also has strong variations during the whole tidal period, as shown by the blue lines in Fig. 3a, c. A typical tidally averaged vertical profile of the eddy viscosity is shown by the red line in Fig. 3a, c.

If the vertical profile of the eddy viscosity is averaged over flood or ebb phase, the difference is quite obvious between the two profiles, which is called the asymmetry. In the model area, the two kinds of the asymmetry, namely the flood-dominated asymmetry and the ebb-dominated asymmetry, both exist (Fig. 3b, d). It appears in Fig. 4 that on both sides of the bay, the flood-dominated asymmetry (negative values in the Fig. 4) appears. While in the deep channel of the bay, the flood-dominated asymmetry and the ebb-dominated asymmetry (positive values in the Fig. 4) appear alternatively. Except at the mouth of the bay where the intensity of the tidal asymmetry of the eddy viscosity on the shoals is bigger than that in the

deep channel, and opposite features of the magnitude of the symmetry exist in the remaining part of the bay. The maximum difference occurs at the head of the bay.

The eddy viscosity coefficients obtained from FVCOM by using the MY-2.5 model are kept based on which three kinds of the eddy viscosity are generated for further comparison. Firstly, the eddy viscosity is averaged temporally in one tidal period on every grid point to get the time invariant eddy viscosity. Then they are averaged vertically in the water column to get the eddy viscosity only varying horizontally. Lastly, the eddy viscosity goes through a further horizontal averaging procedure to get the constant eddy viscosity in the whole model domain. The three kinds of the eddy viscosity are applied in FVCOM to replace the MY-2.5 model. Then the so obtained tidal currents are used to get the LRV. It demonstrates that the structures of the LRV based on these three kinds of the time-invariant eddy viscosity are nearly the same, although the magnitudes of the LRV have a big difference, which will be discussed later. This is because the time-varying characteristic is removed from the eddy viscosity term and its only remaining effect is to damp the LRV. Hence, the structures of the LRV based on the time-invariant eddy viscosity will be compared with those based on the tide-varying eddy viscosity, which will be discussed below to evaluate the effect of the nonlinearity of the eddy viscosity. Considering the generality of the comparison, two bay lengths are chosen, which are 0.3 and 1 wavelength respectively.

For the 0.3 wavelength long bay case, there are significant differences in the LRV at the cross-section of 0.75 bay lengths away from the head between the linear and nonlinear eddy viscosity case. The LRV flows outside from the slope and the lower layers of the deep channel and flows inside from the upper layers of the deep channel and from both sides of the banks when the time-varying eddy viscosity is used (Fig. 5a). While in Fig. 5b–d, if the time-invariant eddy viscosity is adopted, the LRV flows outside from the deep channel and inside from the banks of the bay, which is simpler than that in Fig. 5a. In the inner bay, the direction of the LRV in the MY-2.5 model case is inward at the bottom layers of the deep channel, while for the three time-invariant eddy viscosity cases the LRV is outward and the outflow area becomes bigger with the shift from the tidally averaged case to the constant eddy viscosity case (Fig. 5b–d). It should be noted that the constant eddy viscosity averaged from the output of the MY-2.5 model is 0.0015 m^2/s in this experiment. Thus, the

Fig. 3 The vertical eddy viscosity profiles of two points at the mouth of the bay. The profiles of the point at the center of the deep channel are drawn in **a** and **b**, and the profiles of the point near the bank are drawn in **c** and **d**. In **a** and **c**, the *blue lines* represent the time series of the vertical eddy viscosity profiles in a tidal cycle and the *red lines* represent the tidally averaged eddy viscosity profile; in **b** and **d**, the *red lines* represent the flood-averaged eddy viscosity and the *blue lines* represent the ebb-averaged eddy viscosity
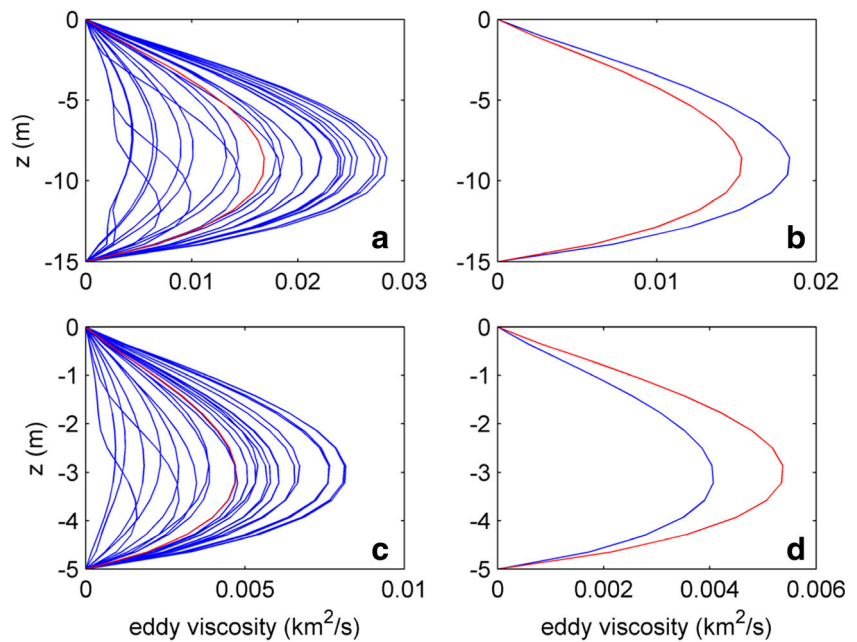
nondimensional parameter δ_e is 0.16, which is one order smaller than that used in Jiang and Feng (2014). Hence, the LRV (in Fig. 5d) is different from those in Fig. 1 which means the magnitude of the eddy viscosity is important to the LRV.

If the bay is one-wavelength long, the structures of the LRV at each section in tidally averaged case are nearly the same, as shown in Fig. 6a, b, with the outward flowing area in the deep channel and the inward flowing area on the shoals. The 3D LRV in the tidally vertically averaged case and in the constant eddy viscosity case almost have the same pattern as that in the tidally averaged case (The figures are omitted).

For the depth-integrated LRV, the LRV flows inside from the both sides and the deep channel and flows outside from the slopes between 0.23 and 0.27 wavelengths away from the head of the 0.3 wavelength long bay exhibited in Fig. 7a, while at the same position of Fig. 7b–d the LRV flows inside from both sides and slopes and outside from the deep channel when the time-invariant eddy viscosity is used. For the one wavelength long bay, a pair of cells flows inside from the deep channel and outside from the slopes and both sides of the bay in the position between 0.5 and 0.6 wavelengths away from the head of the bay in Fig. 8a. In Fig. 8b, the pair of cells disappears and the semi-enclosed cells at the mouth and the cells in the inner bay become bigger and occupy the position when the tidally averaged eddy viscosity is used. The depth-integrated LRV for the other two time invariant eddy viscosity cases almost have the same pattern as that in the tidally aver-aged case (The figures are omitted).

In a 0.3 wavelength long bay when the nonlinear eddy viscosity is used, the breadth-averaged LRV flows inside from the middle and lower layers and outside from the upper layers in the horizontal areas from the head of bay to 0.2 wavelengths

away from it, while the reverse results are obtained near the open boundary (Fig. 9a). In the tidally averaged case and in the tidally-vertically averaged case, the LRV flows toward the sea from the upper layers near the head of the bay and there is an anti-clockwise cell in the middle and bottom layers. From 0.09 to 0.15 wavelengths away from the head of the bay, there exists a clockwise cell. Near the open boundary, an anti-clockwise semi-enclosed cell exists (Fig. 9b, c). While for the constant eddy viscosity case in Fig. 9d, the breadth-averaged LRV flows inside from the upper layers and outside from the lower layers in the whole bay except for the areas near the head.

In a one wavelength long bay, when the nonlinear eddy viscosity is used, there exists a clockwise cell near the head of the bay. Adjacent to it, an anti-clockwise cell exists. At the position which is 0.55 and 0.65 wavelengths away from the head of the bay, a small cell has the same flowing direction with that near the head. At the mouth of the bay, the down-estuary flow exists in the middle and lower layers with the up-estuary flow in the upper layers (Fig. 10a). However, under the tidally averaged case, the structure of the LRV is simple with flowing outside in the middle and bottom layers and inside at the surface (Fig. 10b).

Not only the pattern but also the magnitude of the LRV has the obvious changes when the nonlinear effects of eddy vis-cosity are considered. For a 120-km long bay, the intensity of the dimensional LRV increases as the ratio of the maximum depth in the channel and the minimum depth on the shoal increases. The intensity of the LRV in the tidally averaged case is more than 2 times, 1.5 times, and 1.3 times bigger than that in the MY-2.5 model case with the ratio of the maximum depth in the channel and the minimum depth on the shoal

Table 1 Total tidally averaged energy and its component related to LRV of the three groups of experiments in the three kinds of the topography in the 120 km long bay. TIDE KE represents the total tidally averaged kinetic energy and LRV KE represents the total LRV kinetic energy

| Eddy viscosity + bottom friction	$a = 5$ m, $b = 5$ m			$a = 5$ m, $b = 10$ m			$a = 5$ m, $b = 15$ m		
	TIDE KE (10^{12} J)	LRV KE (10^9 J)	LRV KE/ TIDE KE (%)	TIDE KE (10^{12} J)	LRV KE (10^9 J)	LRV KE/ TIDE KE (%)	TIDE KE (10^{12} J)	LRV KE (10^9 J)	LRV KE/ TIDE KE (%)
a MY-2.5 + quadratic	2.295	0.957	0.04	3.850	3.612	0.09	5.064	6.475	0.13
b Tidally averaged + quadratic	2.670	2.398	0.09	4.450	5.485	0.12	5.941	8.909	0.15
c Tidally-vertically averaged + quadratic	2.810	3.034	0.11	4.282	6.481	0.15	6.265	10.110	0.16
d The constant eddy viscosity + quadratic	6.080	43.110	0.71	9.246	68.48	0.74	14.88	97.510	0.66
e Flood-dominated asymmetry + linear	1.639	0.757	0.05	3.350	2.822	0.08	7.121	14.600	0.20
f Ebb-dominated asymmetry + linear	1.655	2.994	0.18	3.370	5.080	0.15	7.123	11.510	0.16
g MY-2.5 + linear	1.733	0.470	0.03	2.977	1.365	0.05	4.912	2.991	0.06
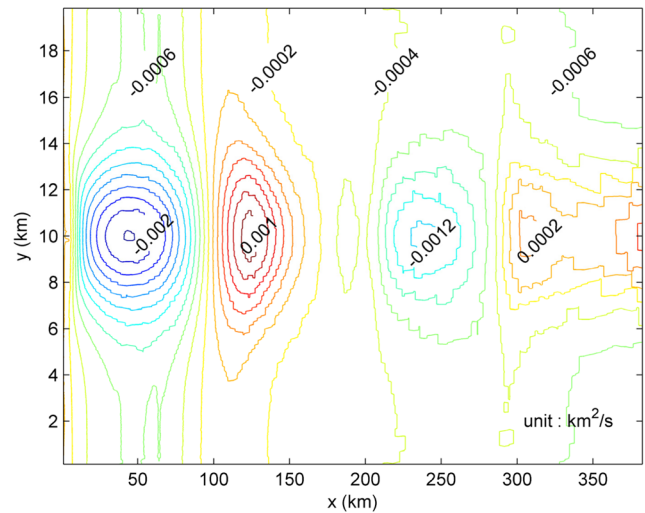
Fig. 4 The deviation of the depth-averaged eddy viscosity between the flood-averaged and the ebb-averaged. The negative value represents the condition that the eddy viscosity during the flood is bigger than that during ebb. The positive value represents the condition that the eddy viscosity during the ebb is bigger than that during the flood

being 2, 3, and 4 (row a and b in Table 1). The change of the LRV intensity in the tidally vertically averaged case is almost the same as that in the tidally averaged case, which shows the vertical distribution of the eddy viscosity has nearly no effects on the LRV (row b and c in Table 1). However, if the eddy viscosity is tidally and spatially averaged in the whole bay, the intensity of the LRV (row d in Table 1) increases by one order compared with that in the MY-2.5 model case (row a in Table 1).

We conclude that the structure of the LRV is highly sensitive to the nonlinear effects of the eddy viscosity in a tidal period. The intensity of the LRV depends not only on the nonlinear eddy viscosity but also on the spatial variation of the eddy viscosity. The intensity of the LRV is highly sensitive to the topography.

3.2 The tidal asymmetry of the eddy viscosity

The different patterns of the tidal asymmetries of the eddy viscosity exist in different regions of the bay because of the tidal nonlinear effects (Cheng et al. 2011). This makes the situation very complex. Cheng et al. (2010) explored the effects of the tidal asymmetry of the eddy viscosity on the breadth-averaged ERV by assuming a simple variation of the eddy viscosity. The similar approach is adopted in this paper to study the influences of the tidal asymmetry of the eddy viscosity on the 3D LRV. Two sensitivity experiments are designed here to represent two different types of the asymmetry, one for the flood-dominated asymmetry (Fig. 11a, the eddy viscosity during flood is larger than that during ebb) and the other for the ebb-dominated asymmetry (Fig. 11b, opposite behavior compared with the flood-dominated

asymmetry). The maximum value of the comparatively higher curved line of the eddy viscosity is $0.02 \text{m}^2/\text{s}$ and that of the lower curved line of the eddy viscosity is $0.01 \text{ m}^2/\text{s}$. They reach the maximum both at the position of $z = -10/15 h_0$ and h_0 is the local depth according to the formula in Ianniello (1977).

The 3D LRV are drawn in Figs. 12 and 13 under different tidal symmetry conditions. Compared with the results in the tidally averaged case (Figs. 5b and 6b), the structures of the LRV are quite different. This is because the eddy viscosity in the two kinds of tidal asymmetry cases varies as the flood phase and the ebb phase changes. Furthermore, the two kinds of the asymmetries of the eddy viscosity have simpler variation than that in the MY-2.5 model case in the tidal cycle, so the LRV in the two cases have different patterns compared with the results in the MY-2.5 model case (Figs. 5a and 6a). It demonstrates that the temporal variation of the eddy viscosity plays the important role in the LRV. The following part will display the effects of the asymmetries of the eddy viscosity on LRV in detail.

For the 0.3 wavelength long bay, as shown in Fig. 12a, the LRV under the flood-dominated asymmetry condition in the upper layers above the slope flows outside and gradually extends to both sides of the banks until the outflow area occupies the banks of the bay from the mouth to the head of the bay. The LRV flows inside from the deep channel and the bottom layers and the inflow area in the upper layers of the deep channel becomes larger and larger from the open boundary to the head of the bay. While in Fig. 12b when the ebb-dominated asymmetry condition is assumed, the outflow is in the lower layers and the outflow area in the lower layers of the banks extends upward until occupying the whole banks from the mouth to the head of the bay, and the inflow area in the upper layers of the deep channel becomes bigger and bigger from the open boundary to the head of the bay. For the one wavelength long bay, compared with that in the 0.3 wavelength long bay, when the position is more than 0.15 wavelengths away from the head of the bay, the 3D LRV flows outside from the upper layers of the banks and inside from the lower layers and the deep channel in the flood-dominated case (Fig. 13a), and the outflow area in the upper layers of the banks becomes larger until they occupy the upper layers from the mouth to the head of the bay. While in the ebb-dominated case (Fig. 13b) the LRV flows outside from the lower layers

Fig. 5 The nondimensional LRV of four cross-sections in the 0.3 wavelength long bay with $a = 5$ m, $b = 10$ m for **a** the MY-2.5 model case, **b** the tidally averaged case, **c** the tidally vertically averaged case, **d** the constant eddy viscosity case with the quadratic bottom friction. The contour interval is 0.02 and the other notions are as in Fig. 1
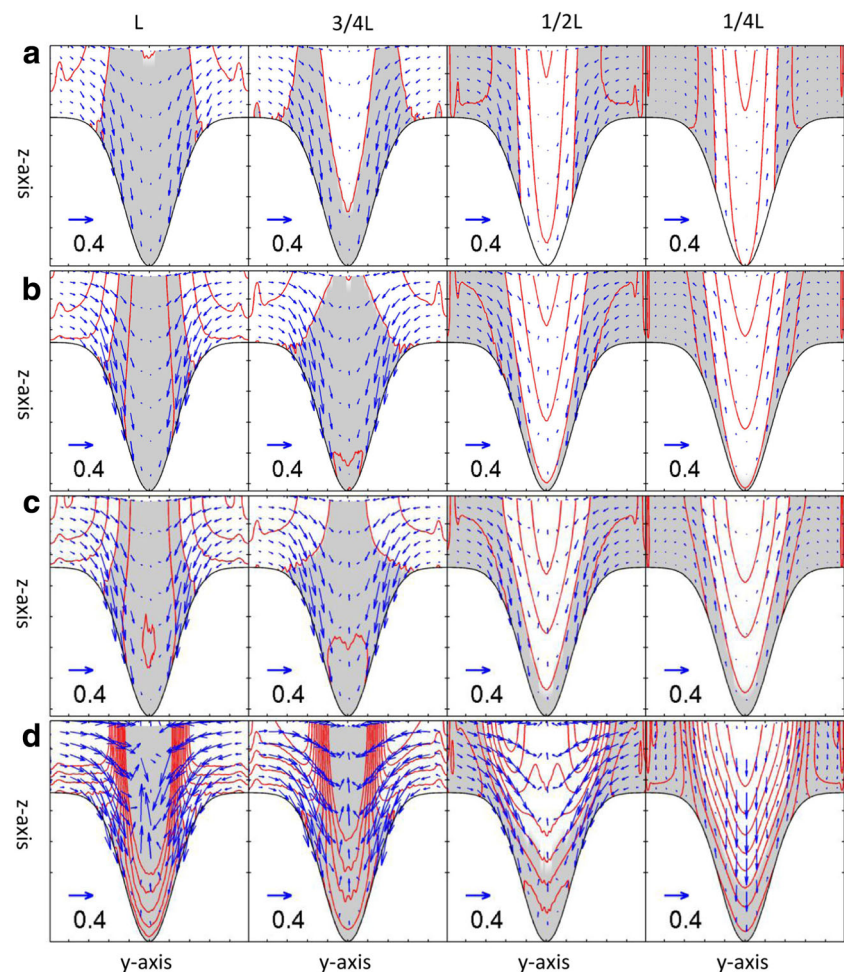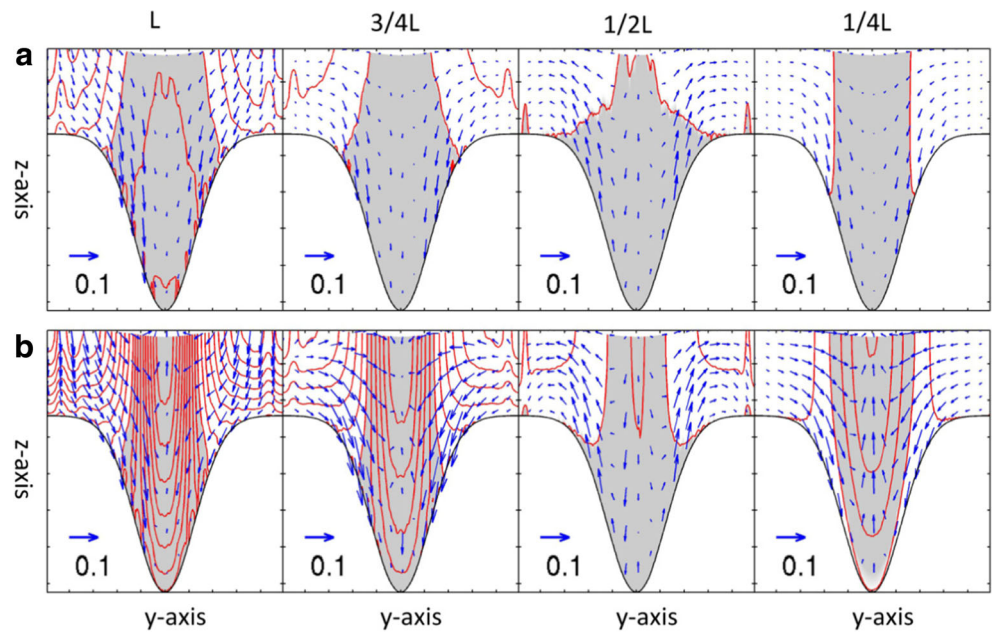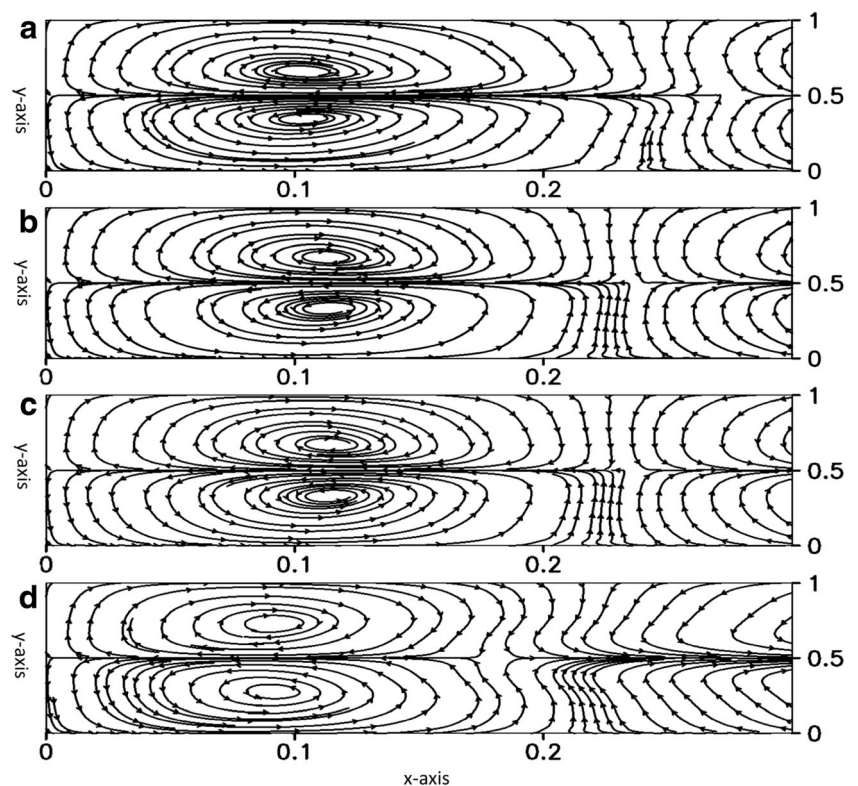
Fig. 6 The nondimensional LRV of four cross-sections in the 1 wavelength long bay with $a = 5$ m, $b = 10$ m for **a** the MY-2.5 model case, **b** the tidally averaged case with the quadratic bottom friction. The contour interval is 0.01 and the other notions are as in Fig. 1

and inside from the upper layers, the outflow area in the lower layers of the banks becomes thinner and that in the lower layers of the deep channel becomes larger from the open boundary to the head of the bay.

The depth-integrated LRV flows inside from the deep channel and outside from the banks (the figures are omitted) and has nearly no changes between the flood-dominated and the ebb-dominated asymmetries. However, the results of the breadth-averaged LRV are significantly sensitive to the tidal asymmetry of the eddy viscosity. For the 0.3 wavelength long bay, as shown in Fig. 14, the LRV under the flood-dominated asymmetry condition has the same pattern as that of the gravitational circulation, while the LRV under the ebb-dominated asymmetry condition is nearly the same as that in Ianniello (1977). Because of the topography, the direction-turning position of the LRV is at the minimum depth. For the one

Fig. 7 The streamlines of the depth-integrated LRV in the 0.3 wavelength long bay with $a = 5$ m, $b = 10$ m for **a** the MY-2.5 model case, **b** the tidally averaged case, **c** the tidally vertically averaged case, **d** the constant eddy viscosity case with the quadratic bottom friction

Fig. 8 The streamlines of the depth-integrated LRV in the 1 wavelength long bay with $a = 5$ m, $b = 10$ m for **a** the MY-2.5 model case, **b** the tidally averaged case with the quadratic bottom friction
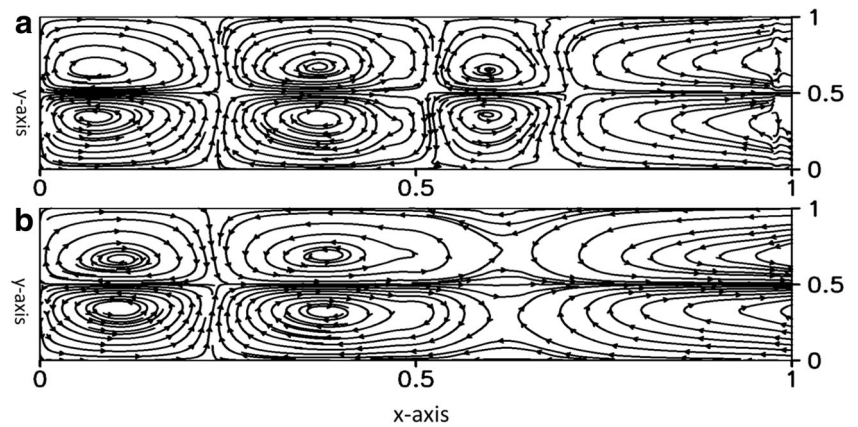
wavelength long, the same results are obtained (the figures are omitted).

The LRV kinetic energy is also affected by the different tidal asymmetries of the eddy viscosity. In the 120-km long bay, the intensity of the LRV for the ebb-dominated case is more than three or two times bigger than that of the flood-dominated case when $b=5$ m or $b=10$ m is set. When $b=15$ m is set, the intensities of the LRV in the two cases are almost the same. In other words, the tidal asymmetry of the eddy viscosity affects not only the pattern of the LRV but also the magnitude of the LRV kinetic energy. Also, the intensity of the LRV highly depends on the topography. However, there are no obvious differences in the effects on the tide between the two cases, which can be seen from the total tidally averaged

kinetic energy listed in row e and f in Table 1 and the figures of co-tide and co-range lines (the figures are omitted).

3.3 Sensitivity to the form of the bottom friction

The nonlinear effects of the bottom friction on the LRV are studied in this section by comparing the results between the linear bottom friction and the quadratic bottom friction in the FVCOM model. In most estuaries, the magnitude of the velocity is in the range of 0.5 to 1 m/s, which implies that the linear bottom friction coefficient ranges from 1.06×10^{-3} to 2.12×10^{-3} m/s, assuming the quadratic bottom friction coefficient $C_d = 0.0025$ (Li and O'Donnell 1997). In this section, the linear bottom friction coefficient is 1.76×10^{-3} m/s. The

Fig. 9 As in Fig. 7 but for the streamlines of the breadth-averaged LRV
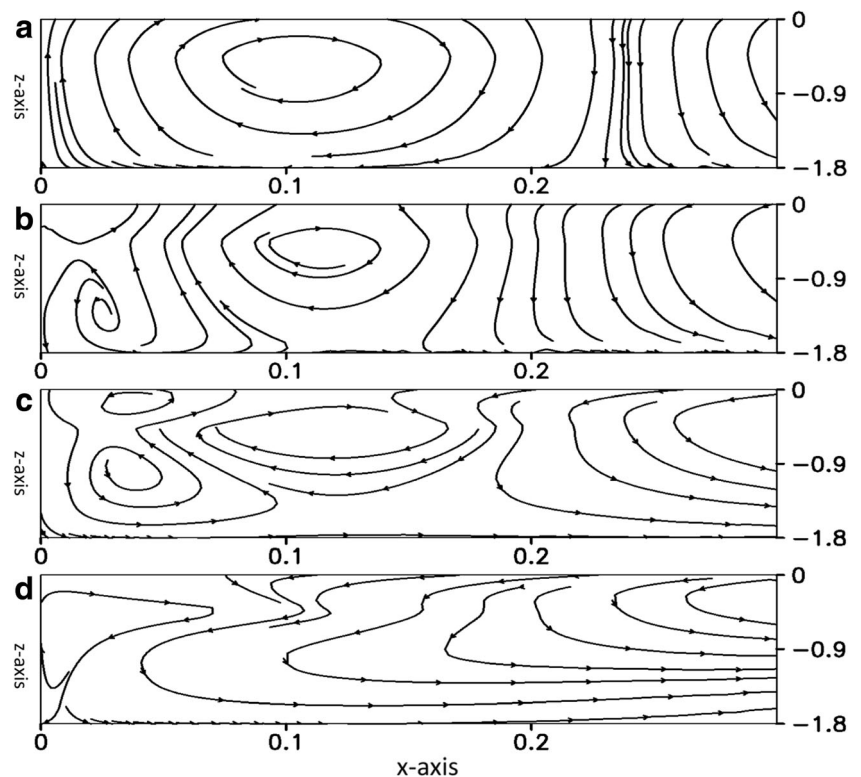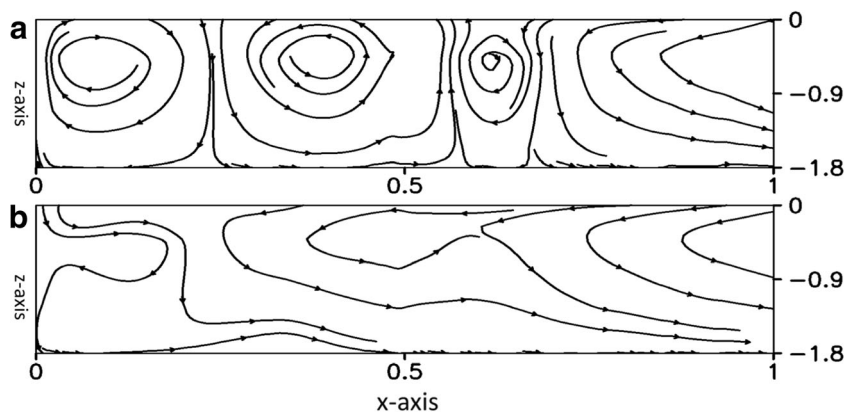
Fig. 10 As in Fig. 8 but for the streamlines of the breadth-averaged LRV in the 1 wavelength long bay

eddy viscosity is calculated by the MY-2.5 turbulence closure model.

When the results of the cross-section are examined, it appears that the LRV flows inside from the deep channel and outside from the bottom layers and the banks with the exceptions for two small areas at both sides of the banks of the outer bay (Fig. 15a, b). While for the results with the quadratic bottom friction (Fig. 5a), it is clear that the LRV has different structures in the inner bay and outer bay in the 0.3 wavelength long bay. This result also shows that the structure of the LRV with the linear bottom friction is simpler than those with the quadratic bottom friction.

The results of the depth-integrated LRV in a 0.3 wavelength long bay with the linear bottom friction are shown in Fig. 16a. It appears that the two cells in the inner bay extend to

the open boundary exhibiting the pattern of flowing inside from the deep channel and outside from the banks of the bay. This pattern is simpler than the results with the opposite flowing directions in the inner bay and the outer bay when the quadratic bottom friction is used (Fig. 7a). In a one wavelength long bay, the structure of the LRV displayed in Fig. 16b is also simpler than the polycyclic structure generated by the quadratic bottom friction (Fig. 8a). The two cells at the head of the bay remain the same as in Fig. 8a with the quadratic bottom friction. However, the two semi-enclosed cells in the outer bay extend to the position of 0.25 wavelengths away from the head of the bay in Fig. 16b with the linear bottom friction being assumed. In-between two small cells between 0.25 and 0.35 wavelengths away from the head have opposite direction compared with those near the head and in the outer bay.

Fig. 11 The vertical profiles of the eddy viscosity (m^2/s) for **a** flood-dominated asymmetry and **b** ebb-dominated asymmetry
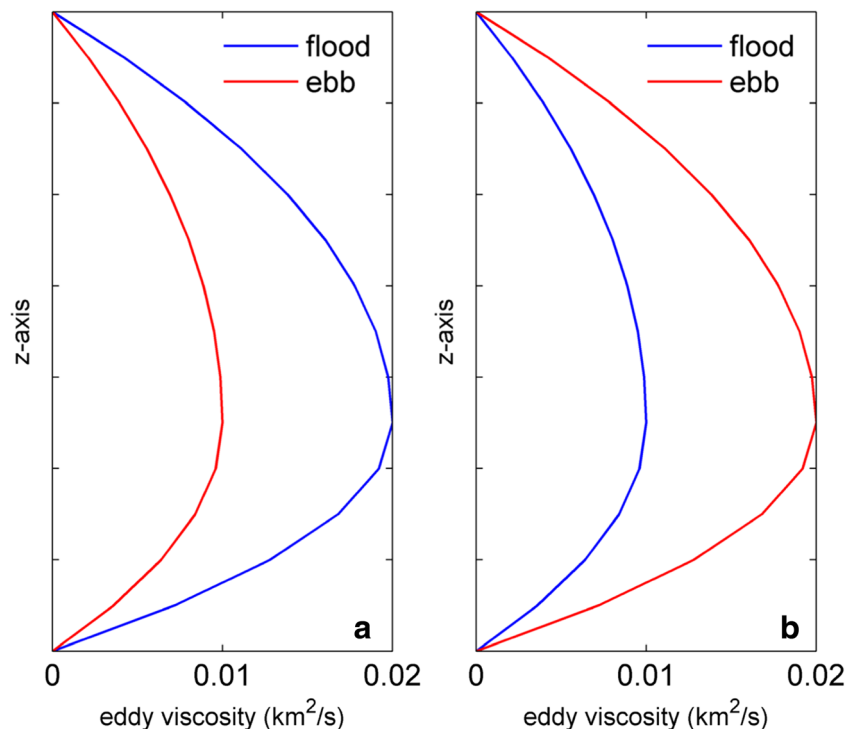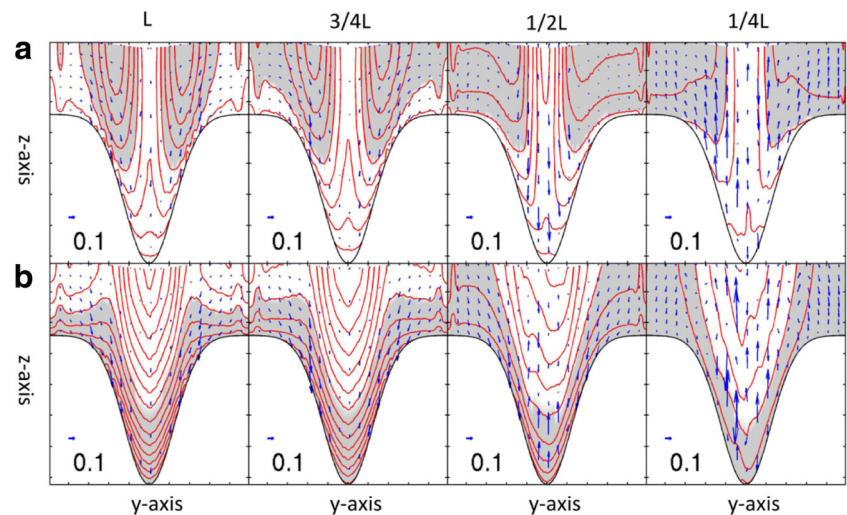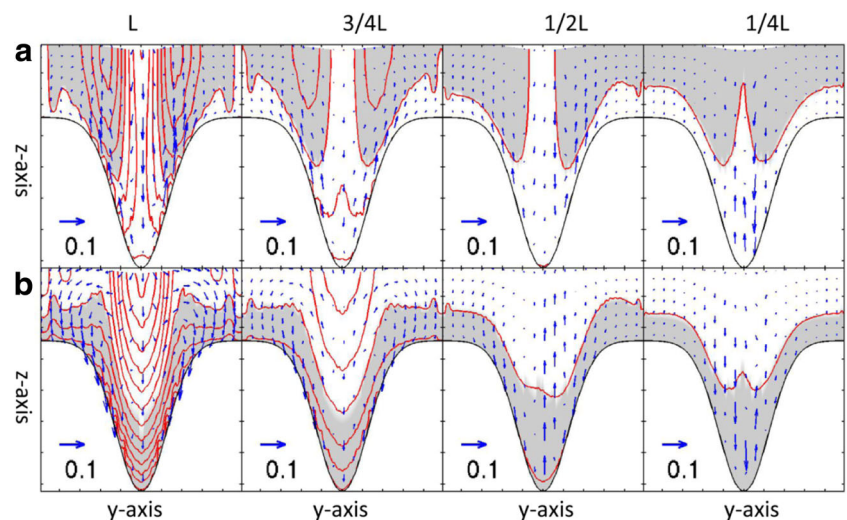
Fig. 12 The nondimensional LRV of four cross sections in the 0.3 wavelength long bay with $a = 5$ m, $b = 10$ m for **a** flood-dominated asymmetry and **b** ebb-dominated asymmetry with the linear bottom friction ($\beta_T = 0.00176$ m/s). The contour interval is 0.01 and the other notions are as in Fig. 1

Not only the pattern but also the intensity of the LRV has obvious changes. The intensity of the LRV in the linear bottom friction case is more than two times smaller than that in the quadratic bottom friction case in all the three kinds of the topography (row g in Table 1). This demonstrates the generation mechanism of the LRV due to the nonlinearity of the bottom friction.

In general, it shows that the form of the bottom friction has obvious influences on the 3D LRV and the depth-integrated LRV. Since the quadratic bottom friction includes both the linear part and the nonlinear part with the linear part dissipating energy and the nonlinear part generating the LRV. Hence, the results with the linear bottom friction are simpler than those with the quadratic bottom friction, which is consistent qualitatively with the depth-averaged analytical results in Jiang and Feng (2011) and numerical results in Quan et al. (2014). However, the breadth-averaged LRV is almost unaffected by changing the form of the bottom friction (the figures are omitted).

4 Conclusions

In this paper, the Lagrangian residual velocity in an idealized bay is calculated according to its definition based on the tidal currents obtained from the FVCOM model. It shows a close agreement between the numerical solution and the analytical solution in Jiang and Feng (2014) when the same setting is used.

Several numerical experiments are carried out to study the effect of the nonlinear eddy viscosity and the influence of the different forms of the bottom friction on LRV in the three kinds of the topography. The results show that the pattern does not change according to the variation of the topography, but the intensity of the LRV increases as the ratio of the maximum depth in the deep channel and the minimum depth on the shoal does. The detailed conclusions are as follows:

The present work overcomes the temporally constant eddy viscosity limitation in the analytical solution by considering the periodic oscillation of eddy viscosity calculated by the

Fig. 13 As in Fig. 12 but for the 1 wavelength long bay

Fig. 14 The streamlines of the breadth-averaged LRV in the 0.3 wavelength long bay with $a = 5$ m, $b = 10$ m for **a** flood-dominated asymmetry and **b** ebb-dominated asymmetry with the linear bottom friction ($\beta_T = 0.00176$ m/s)
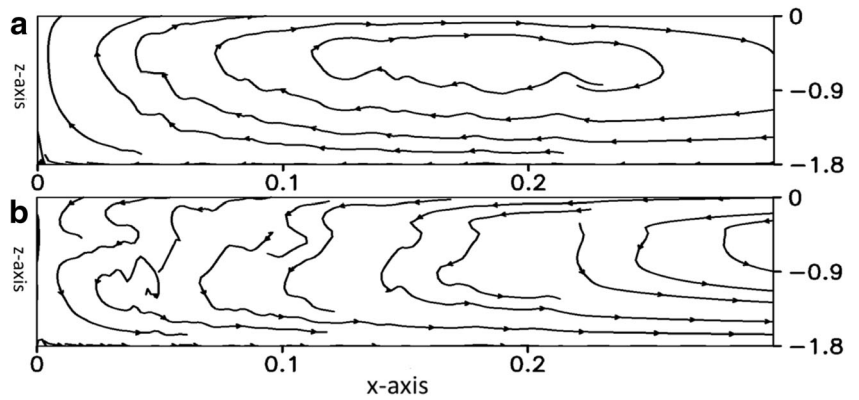
MY-2.5 turbulence closure model. It shows that the LRV patterns are similar when different kinds of the time-invariant eddy viscosity are used in the FVCOM model. The structure is more complex when the time-varying eddy viscosity is used which shows the important effect of the nonlinearity of the eddy viscosity. However, the intensity of the LRV is from 1.3 times to one order bigger when temporally constant eddy viscosity is assumed than those when the time varying eddy viscosity is used under the three kinds of the topography.

The tidal asymmetry of the eddy viscosity during the flood and ebb is a typical type of the nonlinear eddy viscosity. Two sensitivity experiments are designed to study the effects of the two kinds of the asymmetry of eddy viscosity on the LRV. It appears that the 3D LRV has opposite patterns except for the

Fig. 15 The nondimensional LRV of four cross sections in **a** the 0.3 wavelength long bay and **b** the 1 wavelength long bay with $a = 5$ m, $b = 10$ m for the MY-2.5 model case with the linear bottom friction ($\beta_T = 0.00176$ m/s). The contour interval is 0.02 and 0.01, respectively, in (**a**) and (**b**). The other notions are as in Fig. 1
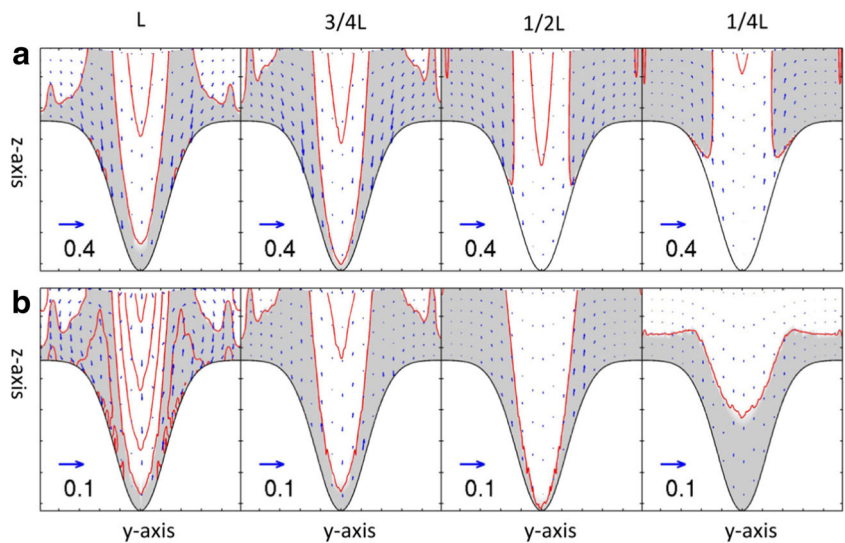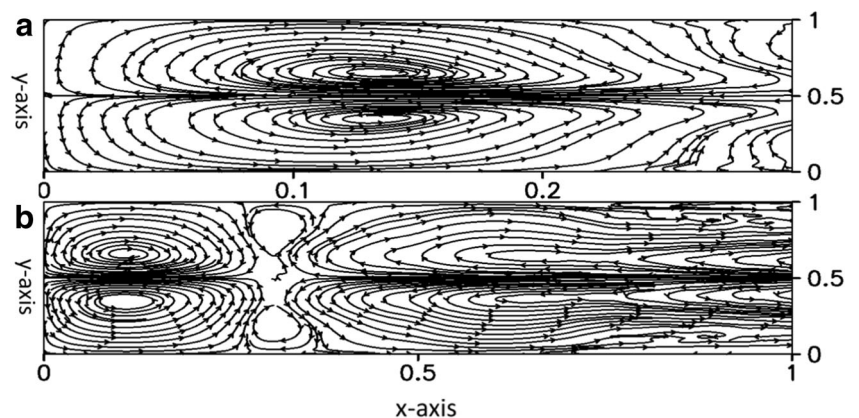

Fig. 16 The streamline of the depth-integrated LRV for **a** the 0.3 wavelength long bay and **b** the 1 wavelength long bay with $a = 5$ m, $b = 10$ m for the MY-2.5 model case with the linear bottom friction ($\beta_T = 0.00176$ m/s)

upper layers of the deep channel in the cross-sections which are more than 0.15 wavelengths away from the head of the bay. The depth-integrated LRV is not sensitive to the asymmetry of the eddy viscosity, while the structures of the breadth-averaged LRV are opposite in the two experiments. The ratio of the intensity of the ebb-dominated asymmetry case and that of the flood-dominated case decreases by from more than three times to one time as the ratio of the maximum depth in the deep channel and the minimum depth on the shoal increases by from two to four times.

The nonlinear effects of the bottom friction on the LRV are studied in this paper to relieve the limitation of the analytical solution (Winant 2008; Jiang and Feng 2014). The form of the bottom friction has significant influences on the 3D LRV and the depth-integrated LRV, while the breadth-averaged LRV is not sensitive to the form of the bottom friction. The intensity of the LRV in the quadratic bottom friction case is more than two times bigger than that in the linear bottom friction case in the three kinds of the topography.

In this paper, only the barotropic condition is considered the effect of the nonlinearity of the eddy viscosity is obvious, yet the baroclinic condition will give more complexity to the variation of the eddy viscosity. Therefore, it will be studied in the future to give deeper understanding of the generation mechanism of the 3D LRV.

References

Abbott MR (1960) Boundary layer effects in estuaries. J Mar Res 18:83–100

Burchard H, Hetland RD (2010) Quantifying the contributions of tidal straining and gravitational circulation to residual circulation in periodically stratified tidal estuaries. J Phys Oceanogr 40:1243–1262. doi:10.1175/2010JPO4270.1

Burchard H, Schuttelaars HM (2012) Analysis of tidal straining as driver for estuarine circulation in well mixed estuaries. J Phys Oceanogr 42:261–271. doi:10.1175/JPO-D-11-0110.1

Burchard H, Hetland RD, Schulz E, Schuttelaars HM (2011) Drivers of residual estuarine circulation in tidally energetic estuaries: straight and irrotational channels with parabolic cross section. J Phys Oceanogr 41:548–570. doi:10.1175/2010JPO4453.1

Burchard H, Schulz E, Schuttelaars HM (2014) Impact of estuarine convergence on residual circulation in tidally energetic estuaries and inlets. Geophys Res Lett 41:913–919. doi:10.1002/2013GL058494

Chen CS, Liu HD, Beardsley RC (2003) An unstructured grid, finite-volume, three-dimensional, primitive equations ocean model: application to coastal ocean and estuaries. J Atmos Ocean Technol 20:159–186. doi:10.1175/1520-0426(2003)020<0159:AUGFVT>2.0.CO;2

Cheng P (2014) Decomposition of residual circulation in estuaries. J Atmos Ocean Technol 31:698–713. doi:10.1175/JTECH-D-13-00099.1

Cheng P, Valle-Levinson A, de Swart HE (2010) Residual currents induced by asymmetric tidal mixing in weakly stratified narrow estuaries. J Phys Oceanogr 40:2135–2147. doi:10.1175/2010JPO4314.1

Cheng P, Valle-Levinson A, de Swart HE (2011) A numerical study of residual circulation induced by asymmetric tidal mixing in tidally dominated estuaries. J Geophys Res 116:642–653. doi:10.1029/2010JC006137

Cheng P, de Swart HE, Valle-Levinson A (2013) Role of asymmetric tidal mixing in the subtidal dynamics of narrow estuaries. J Geophys Res 118:2623–2639. doi:10.1002/jgrc.20189

Feng SZ, Lu YY (1993) A turbulent closure model of coastal circulation. Chin Sci Bull 38:1737–1741

Feng SZ, Cheng RT, Xi P (1986a) On tide-induced Lagrangian residual current and residual transport 1. Lagrangian residual current. Water Resour Res 22:1623–1634. doi:10.1029/WR022i012p01623

Feng SZ, Ju L, Jiang WS (2008) A Lagrangian mean theory on coastal sea circulation with inter-tidal transports. I. Fundamentals. Acta Oceanol Sin 27:1–16. doi:10.3969/j.issn.0253-505X.2008.06.001

Hansen DV, Rattray MJ (1965) Gravitational circulation in straits and estuaries. J Mar Res 23:104–122

Ianniello JP (1977) Tidally induced residual currents in estuaries of constant breadth and depth. J Mar Res 35:755–786

Jay DA, Musiak JD (1994) Particle trapping in estuarine tidal flows. J Geophys Res 99:20445–20461. doi:10.1029/94JC00971

Jay DA, Musiak JD (1996) Internal tidal asymmetry in channel flows: origins and consequences. In: Pattiaratchi C (ed) Mixing in estuaries and coastal seas. Coastal and Estuarine Studies. American Geophysical Union, Washington, pp 211–249

Jiang WS, Feng SZ (2011) Analytical solution for the tidally induced Lagrangian residual current in a narrow bay. Ocean Dyn 61:543–558. doi:10.1007/s10236-011-0381-z

Jiang WS, Feng SZ (2014) 3D analytical solution to the tidally induced Lagrangian residual current equations in a narrow bay. Ocean Dyn 64:1073–1091. doi:10.1007/s10236-014-0738-1

Lamb H (1975) Hydrodynamics. Cambridge University Press, London

Li CY, O'Donnell J (1997) Tidally driven residual circulation in shallow estuaries with lateral depth variation. J Phys Oceanogr 27:915–927. doi:10.1029/97JC02330

Mellor GL, Yamada T (1982) Development of a turbulence closure model for geophysical fluid problems. Rev Geophys 20:851–875. doi:10.1029/RG020i004p00851

Quan Q, Mao XY, Jiang WS (2014) Numerical computation of the tidally induced Lagrangian residual current in a model bay. Ocean Dyn 64:471–486. doi:10.1007/s10236-014-0696-7

Simpson JH, Brown J, Matthews J, Allen G (1990) Tidal straining, density currents, and stirring in the control of estuarine stratification. Estuaries 13:125–132. doi:10.2307/1351581

Winant CD (2008) Three-dimensional residual tidal circulation in an elongated, rotating basin. J Phys Oceanogr 38:1278–1295. doi:10.1175/2007JPO3819.1

Zimmerman JTF (1979) On the Euler-Lagrange transformation and Stokes' drift in the presence of oscillatory and residual currents. Deep-Sea Res 26A:505–520. doi:10.1016/0198-0149(79)90093-1